Correspondence to:

E. Caspari,
eva.caspari@unileoben.ac.at

Mechanical Compliance of Individual Fractures in a Heterogeneous Rock Mass From Production-Type Full-Waveform Sonic Data

Zhenya Zhou[1] , Eva Caspari[2] , Nicolás D. Barbosa[1] , Andrew Greenwood[1,2] , and Klaus Holliger[1]

[1]Institute of Earth Sciences, University of Lausanne, Lausanne, Switzerland, [2]Chair of Applied Geophysics, Montanuniversität Leoben, Leoben, Austria

Abstract The mechanical fracture compliance is of interest in a number of geoscientific applications. Seismic borehole methods, especially full-waveform sonic (FWS) data, have indicated their potential to infer the compliance of macroscopic fractures under in situ conditions. These approaches rely on the assumption of a homogeneous background embedding the fractures and, as of yet, compliance estimates for individual fractures are limited to static FWS measurements. In this work, we assess the potential of inferring the compliance of individual fractures from standard, production-type FWS data in the presence of background heterogeneity. We first perform a comparative test on synthetic data to evaluate three approaches known as the transmission, phase, and group time delay methods. The results indicate that the former two produce adequate compliance estimates for scenarios with a strongly heterogeneous background or a damage zone around the fracture. These two methods are then applied to two FWS data sets acquired before and after a hydraulic stimulation campaign in a crystalline rock, which allows to test them on natural and man-made fractures. The transmission method turned out to be unsuitable for the considered data due to its reliance on amplitudes. Conversely, the travel time behavior remained stable and the phase time delay method produced robust and consistent estimates. The results for a newly created hydro-fracture imply the capability of resolving remarkably small compliance values of the order of 10^{-14} m/Pa. This estimate is one order-of-magnitude smaller than that for the natural fracture, which may help to distinguish between these two fracture types.

Plain Language Summary Fracture characterization is of interest in a number of geoscientific applications. Seismic borehole methods in general and sonic log measurements in particular have the potential to infer an important mechanical fracture property, known as compliance, under in situ conditions. These methods exploit that fractures reduce amplitudes and delay the travel times of seismic waves and rely on the assumption of a homogeneous embedding rock mass. Here, we assess the potential of inferring compliance from standard, production-type sonic data in the presence of background heterogeneity. We first perform a modeling study to evaluate two methods based only on travel-time delays and one accounting additionally for the amplitude decay. The latter and one of the time delay methods produce adequate results for heterogeneous scenarios. These two methods are then applied to data sets acquired before and after small man-made fractures were created. The amplitude method turned out to be unsuitable due to inconsistencies in the amplitudes, whereas the time delay method produced reliable estimates. The results for the man-made fracture demonstrate the capability of resolving compliance values that are much smaller than those of natural fractures. This may open the perspective of using this technique to distinguish between natural and man-made fractures.

1. Introduction

The presence of fractures, which are typically hydraulically much more transmissive and mechanically much more compliant than their embedding background, is ubiquitous throughout the upper crust (e.g., Barton, 2006). Correspondingly, there is increasing interest not only in the detection, but also, and in particular, in the geometrical, mechanical, and hydraulic characterization of fractures for a wide range of applications throughout the Earth, environmental, and engineering sciences, such as, for example, hydrocarbon exploration (e.g., Sayers, 2007), geothermal energy production (Vidal & Genter, 2018), groundwater and contaminant hydrogeology (Ofterdinger et al., 2019; Pyrak-Nolte & Nolte, 2016), hydraulic fracturing and shearing (e.g., Tran & Rahman, 2007). Fractures can be detected and characterized through direct and indirect observations. Indirect approaches of fracture

detection and characterization, which rely on geophysical remote-sensing-type techniques in general and seismic methods in particular, are becoming increasingly important due to their ability to provide spatial information about geometrical and physical attributes of fractured rock masses at the field scale (e.g., Clark et al., 2009; Day-Lewis et al., 2017). However, the interpretation of typical seismic data is mostly limited to estimates of the effective or "average" mechanical behavior and geometrical characteristics of the entire probed fractured rock mass and, hence, does not provide insights into the properties of individual fractures (e.g., Vasconcelos & Grechka, 2007). Direct observations, on outcrops, along tunnels, on drill cores or from electrical, optical, and acoustic televiewer logs can provide detailed information about geometrical characteristics of fractures and fracture networks (e.g., Williams & Johnson, 2004), while the mechanical and hydraulic characteristics of fractures generally need to be inferred from dedicated laboratory and field measurements (e.g., Minato & Ghose, 2016; National Research Council, 1996; Prioul & Jocker, 2009). Laboratory experiments are typically employed to obtain the mechanical compliance (Möllhoff et al., 2010; Pyrak-Nolte, 1996) and permeability of fractures (e.g., Ye et al., 2017) under well-controlled conditions (e.g., stress state, temperature, fluid saturation, geometrical characteristics). However, they are generally limited by the small scale of the samples, the number of available specimens, deviations from the underlying in situ conditions, or the man-made origin of the fractures. As such, one cannot directly extrapolate laboratory results to more complex fracture networks and environments (e.g., Barton, 2006).

Given the aforementioned limitations for laboratory measurements, knowledge of mechanical properties of individual natural fractures under in situ conditions is, thus, essential to upscale laboratory observations to the field scale. Borehole seismic methods and especially full-waveform sonic (FWS) data have the potential to bridge this gap in scale and resolution, as they provide the possibility to directly access and characterize the mechanical response of individual fractures under well-controlled in situ conditions (Barbosa et al., 2019). Despite the fact that there is typically still an order-of-magnitude-type difference between the apertures of fractures and the prevailing seismic wavelengths in borehole experiments, it has been observed experimentally and reconciled theoretically that individual fractures have a determining impact on seismic wave propagation (e.g., Pyrak-Nolte et al., 1990; Schoenberg, 1980). The overall effects of fractures on seismic waves are to reduce their amplitudes and to delay their travel times. These observables are in direct relation with the mechanical compliance of fractures, which quantifies the deformation of a fracture upon loading (e.g., Möllhoff et al., 2010).

The estimation of the compliance of individual fractures can be valuable not only for the mechanical characterization of the rock mass but may also provide insights into the hydraulic properties, hydromechanical interactions, and stress sensitivity of fractures (e.g., Pyrak-Nolte & Nolte, 2016; Rutqvist & Stephansson, 2003; Schmidt et al., 2022). As the mechanical compliance affects fracture deformation in response to changes in effective stress, in particular, the opening and closing pressures, its knowledge can play a role for diagnostic fracture injection tests to determine the in situ stress (e.g., McClure et al., 2016) and for hydraulic stimulation experiments and potentially associated induced seismicity in general (e.g., Davies et al., 2013; Shapiro & Dinske, 2009). The implicit link between fracture compliance and hydraulic transmissivity (Barbosa et al., 2021; Pyrak-Nolte & Nolte, 2016), on the other hand, is related to the fact that both properties depend on similar geometrical features, such as the aperture distribution, roughness of the fracture surfaces, and the fracture length (e.g., Gutierrez & Youn, 2015; Lissa et al., 2019; Liu, 2005; Pyrak-Nolte & Morris, 2000). In this context, understanding the difference between the compliance-transmissivity relation for natural and man-made macro-fractures is of particular interest, although related evidence is still sparse (Prioul & Jocker, 2009). Stimulation boreholes containing pre-existing fractures represent an ideal scenario to explore these differences as they allow to quantify hydraulic and mechanical properties of both natural and induced fractures.

In this work, we focus on the mechanical response of individual fractures. FWS experiments in boreholes have associated wavefield components, such as, for example, critically refracted P- and S-waves, Stoneley waves, and tube waves, which have proven to be highly sensitive to the mechanical compliance of individual fractures (e.g., Bakku et al., 2013). Barbosa et al. (2021) proposed a method for inferring the normal fracture compliance based on the computation of a complex-valued transmission coefficient from fracture-related phase time delays and amplitude decays of the critically refracted P-wave. The imaginary component of the complex-valued compliance inferred by the transmission method allows to quantify the fracture-related energy dissipation, for example, due to fluid pressure diffusion (FPD) effects and scattering (e.g., Caspari et al., 2019; Rubino et al., 2015; Sotelo et al., 2021). A crucial aspect of the transmission scheme is the concept of a so-called reference trace comprising the critically refracted P-wave from a representative intact section of the background embedding the studied

fracture. The phase delay and the amplitude decay between this reference signal and the P-waves transmitted across a fracture can then be attributed to the presence of the compliant fracture. In addition to a representative section of the host rock, this also requires good repeatability of the source signal and a high signal-to-noise ratio (S/N). The latter is the reason why Barbosa et al. (2021) focused on the so-called static FWS data, for which the tool is stopped during acquisition.

A disadvantage of static FWS experiments is that they are very time-consuming and logistically cumbersome and, hence, generally only feasible over a limited depth range. In this study, we explore whether and under which conditions fracture compliance estimates of individual fractures are possible from standard, production-type FWS data whose S/N are inherently much lower than those of their static counterparts. Given that amplitudes of seismic waves are typically more susceptible to noise than their travel times, we consider, in addition to the transmission method, two compliance estimation methods based solely on travel times (e.g., Pyrak-Nolte, 1996), which are referred to as time delay methods in the following. In analogy to the transmission method, the fracture-induced time delays are also obtained based on the comparison of the critically refracted P-wave across a fracture with a corresponding reference signal. An implicit underlying assumption is that the host rock, where the reference signal is acquired, is quasi-homogeneous. However, heterogeneity is pervasive in the Earth's upper crust, occurs on multiple scales (e.g., Holliger, 1996), and affects both the amplitudes and the travel times of seismic waves (e.g., Aki & Richards, 1980; Holliger, 1997; Müller et al., 1992). While it is reasonable to assume that the reference signal is affected by the heterogeneity of the embedding background, the implications for fracture compliance estimation are unknown. A specific type of heterogeneity associated with fractures is their damage zone (DZ) (e.g., Faulkner et al., 2011). Sotelo et al. (2021) pointed out that the presence of a DZ and associated enhanced FPD between the fracture and the embedding background increase the P-wave reflectivity and, hence, reduce the P-wave transmissivity of fractures. The corresponding impact on fracture compliance estimation from transmission or time delay methods is as of yet unexplored.

The aim of this study is twofold: (a) a comparison of the transmission and time delay approaches to estimate fracture compliance in the presence of background heterogeneity and (b) the assessment of the robustness of fracture compliance estimation for standard, production-type FWS logging data. The paper is structured as follows. First, we describe briefly the transmission scheme and the time delay methods to estimate fracture compliance. We then perform a numerical modeling study to test these methods on synthetic FWS data for pertinent models containing background heterogeneity. Finally, we perform an analysis of the applicability of the considered methods to observed standard, production-type FWS measurements. To do so, we utilize two data sets, one acquired before and one acquired after a "mini-frac" hydraulic stimulation experiment. This allows us to test the robustness of the methods and to quantify and analyze the differences between the compliance of pre-existing natural fractures and newly generated man-made fractures.

2. Methodological Background

The presence of fractures slows the propagation of passing seismic waves and reduces their amplitudes (e.g., Pyrak-Nolte et al., 1990). These effects are mainly controlled by the mechanical compliance of fractures, which, in turn, makes it possible to estimate this important medium property from seismic data. In this study, the seismic experiment considered to illustrate this is typically referred to as FWS logging, which consists of generating pressure waves in the upper sonic frequency range (∼1–50 kHz) at the center of a fluid-filled borehole. The associated wavefield then propagates through the adjacent formation before being recorded by the pressure sensors of the logging tool. In particular, we focus on the critically refracted P-wave, which typically represents the first arriving signal in FWS experiments. By analyzing its travel time and amplitude characteristics, it is feasible to estimate the compliance of fractures lying on its path (e.g., Barbosa et al., 2019, 2021).

Schoenberg (1980) proposed the so-called linear slip model, which assumes that the stress across a fracture is continuous, but not the displacement. The normal fracture compliance connects the normal stress loaded by a propagating wave on the fracture surface with the displacement jump across it. Based on the linear slip model, Barbosa et al. (2021) proposed a transmission method, which combines both the fracture-induced phase delay and amplitude decay of the critically refracted P-wave, to obtain the transmission coefficient T of the normally incident P-wave

$$T(\omega) = e^{-\ln\left(A^{\mathrm{int}}/A^{\mathrm{fra}}\right)+i\omega t_{ph}}, \tag{1}$$

from which one can then infer the complex-valued fracture compliance Z under the assumption of normal incidence (Schoenberg, 1980)

$$Z(\omega) = \frac{2(1-T)}{iT\omega I}. \tag{2}$$

A^{int} and A^{fra} correspond to the amplitudes of the critically refracted P-waves at a specific angular frequency ω after propagating through the intact and fractured sections of the probed subsurface region, respectively. I denotes the acoustic impedance of the intact background rock. For scenarios with a heterogeneous background, the mean P-wave velocity and density are used to compute the impedance. The phase time delay t_{ph} is related to the phase shift $\delta\theta$ between the propagating P-waves through the intact θ^{int} and fractured θ^{fra} sections as

$$t_{ph} = \frac{\delta\theta}{\omega} = \frac{\theta^{\text{fra}}(\omega) - \theta^{\text{int}}(\omega)}{\omega}. \tag{3}$$

All parameters in Equations 1–3 are evaluated in the frequency domain and, hence, the Fourier transform is applied to the refracted P-waves to obtain the associated amplitude and phase spectra. A critical aspect of the transmission method of Barbosa et al. (2021) is that the amplitude decay due to geometrical spreading is assumed to be similar for the intact and fractured sections along the borehole. In this scenario, the amplitude decay between the reference traces obtained from an intact section and those of the P-wave transmitted across a fracture can be attributed mainly to the effects of energy conversion into reflected and transmitted waves at the fracture. In this context, it is important to note that fracture compliance estimates obtained through the transmission method are inherently complex-valued, with the imaginary component being indicative of fracture-related energy dissipation, for example, due to FPD or scattering.

In general, the amplitudes of seismic waves are more susceptible to noise than their phases. Based on evidence from laboratory experiments, Möllhoff et al. (2010) pointed out that the amplitudes of source signals tend to be less repeatable than their phases, which, in turn, poses problems for the accuracy of the transmission method. For this reason, we investigate two alternative methods based on group and phase time delays to estimate the real-valued part of the fracture compliance. These two methods also rely on the concept of a reference signal from a representative intact section along the borehole. Using the linear slip model, Pyrak-Nolte (1996) derived the following relation between the fracture compliance and the associated P-wave group time delay t_g at normal incidence

$$t_g(\omega) = t_{\text{fra}}(\omega) - t_{\text{int}}(\omega) = \frac{d}{d\omega}\delta\theta(\omega) = \frac{2/ZI}{(2/ZI)^2 + \omega^2}. \tag{4}$$

Equation 4 assumes that the travel time of a P-wave propagating across a fracture t_{fra} is equal to the travel time through the intact formation t_{int} plus the fracture-induced time delay t_g, which is conceptually in agreement with the transmission method. The associated fracture-induced phase time delay t_{ph} is given by Möllhoff and Bean (2009)

$$t_{ph}(\omega) = \frac{\delta\theta(\omega)}{\omega} = \frac{1}{\omega}\arctan\left(\frac{\omega ZI}{2}\right). \tag{5}$$

Note that following the outcomes of Möllhoff et al. (2010), the time delays are evaluated in the frequency domain. By rearranging Equations 4 and 5, the dependencies of the fracture normal compliance on the group and phase delays, respectively, can be expressed as

$$Z^g(\omega) = \frac{4t_g}{\left[1 \pm \sqrt{1 - 4t_g^2\omega^2}\right]I}, \tag{6}$$

$$Z^{ph}(\omega) = \frac{2\tan(t_{ph}\omega)}{\omega I}, \tag{7}$$

where the superscripts g and ph denote the fracture compliance associated with the group and phase time delay methods, respectively. The fact that group time delays are not a monotonically changing function of compliance

leads to two possible solutions and makes the estimation of compliance ambiguous (Appendix A). One way to choose between the two solutions is to take the one closest to the phase time delay.

While a common assumption for all schemes considered is that the critically refracted P-wave impinges normally on the fractures, there is evidence to suggest that the transmission method remains valid from small to moderate incidence angles (Barbosa et al., 2019). For the idealized situation of a homogeneous background, upon which the considered compliance estimation techniques are based, the observed differences in terms of time delays and amplitudes decays A^{int}/A^{fra} with regard to the reference traces can be exclusively attributed to the presence of fractures. However, even in the absence of fractures, upper crustal rocks tend to be inherently heterogeneous over a wide range of scales (e.g., Holliger, 1996), the impact of which on the reference signals and, correspondingly, on the compliance estimates remains as of yet unexplored. In the following, we, therefore, assess such effects on the transmission and time delay methods in the framework of a modeling study.

3. Impact of Heterogeneity on Fracture Compliance Estimates: Tests on Synthetic Data

To assess the performance of the three methods outlined above in the presence of a heterogeneous background, we conduct a canonical modeling study. The synthetic data sets are generated using a pseudo-spectral staggered-grid finite-difference solution of Biot's (1962) equations of poroelasticity in cylindrical coordinates (Sidler et al., 2013, 2014). This discretization method requires approximately five grid points per minimum wavelength to control numerical errors related to grid dispersion. The considered cylindrically symmetric numerical models consist of a water-filled domain, representing a borehole with a radius of 7.5 cm, surrounded by a poroelastic medium measuring 5 and 2 m in the vertical and radial directions, respectively. The grid spacing is 2.5 mm in the vertical direction and ranges from 1.1 to 11.2 mm in the radial direction. We consider a horizontal water-saturated fracture, which is part of the poroelastic continuum and characterized by a very low stiffness, that is, by very low bulk and shear moduli, as well as by a very high porosity and permeability with respect to the embedding background. The tortuosity of the fracture does not affect the physical phenomena of interest in this study because the numerical code considers the permeability to be static, rather than a dynamic, property (Pride, 2005; Sidler et al., 2014). Conversely, the stability of our numerical simulations depends on the ratio between the porosity and the tortuosity, which needs to stay within a physically reasonable range. For the fractures, we found that is the case when retaining a similarly high value of the tortuosity as for the embedding background. The source is located in the center of the water-filled borehole at a depth of 0.25 m and emulates a monopole-type transmitter with a dominant frequency of 20 kHz and the time-history of a Ricker wavelet. The receivers, which record the fluid pressure, are spaced at 2.5 mm intervals along the borehole axis. The reference signals for a given source-receiver offset are obtained from separate simulations for intact models without the horizontal fracture. In contrast to observed FWS records, which comprise multiple source positions along the borehole for a small number of receivers, a single source gather with an extended receiver line is simulated. While this experimental setup is a concession to the highly computational cost of the modeling approach, it retains all essential features for assessing the considered fracture compliance estimation methods.

3.1. Model Parameterization

We consider the following canonical models to assess the robustness of the compliance estimation methods in the presence of a heterogeneous background: (a) a stochastically heterogeneous background containing a horizontal fracture without a DZ and (b) a homogeneous background containing a horizontal fracture with a DZ. The results for these models will be compared with those of a reference case of a homogeneous background containing a horizontal fracture without a DZ.

The material properties of the fracture, its embedding background, and the saturating pore fluid are summarized in Table 1. The fracture permeability is based on the cubic law $k^f = h^2/12$, with h denoting the aperture (e.g., Witherspoon et al., 1980). The physical properties of the background emulate a stiff crystalline rock of low porosity and permeability. The grain and fluid properties are the same for the background and the embedded fracture. For the first scenario involving a heterogeneous background, we consider a band-limited self-similar model with Gaussian fluctuations of the elastic moduli and porosity around the mean values of the homogeneous reference model (e.g., Holliger, 1996). The fluctuations are characterized by a von Karman autocovariance function with a

Table 1
Physical Properties of the Embedding Background, Fracture, and Saturating Pore Fluid

Physical property	Background rock				Fracture
		Heterogeneous		Damage zone	-
-	Homogeneous	Mean value	Standard deviation		
Dry frame bulk modulus K_m (GPa)	33	33	3	16.8	0.56
Dry frame shear modulus μ_m (GPa)	29	29	2	14.7	0.33
Porosity ϕ (-)	0.004	0.004	0.001	0.1	0.6
Solid grain bulk modulus K_s (GPa)	37	37	0	37	37
Solid grain density ρ_s (Kg/m^3)	2,730	2,730	0	2,730	2,730
Fluid bulk modulus K_f (GPa)	2.25	2.25	0	2.25	2.25
Fluid density ρ_f (Kg/m^3)	1,000	1,000	0	1,000	1,000
Fluid viscosity μ (Pa s)	0.001	0.001	0	0.001	0.001
Permeability k (Darcy)	5×10^{-4}	5×10^{-4}	0	5×10^{-2}	2.1×10^6
Tortuosity S [-]	2.0	2.0	0	2.0	2.2
Aperture h (mm)	-	-	-	-	5
Length L (m)	2	2	0	2	2

Hurst number of 0.2 and a horizontal-to-vertical aspect ratio of 4 (e.g., Tronicke & Holliger, 2005). The standard deviations of the background porosity and the dry frame bulk and shear moduli are chosen such that the P-wave velocity distribution emulates that of the field FWS data acquired in a crystalline environment (Figure 1). The second scenario consists of a homogeneous background containing a fracture that is surrounded by a homogeneous DZ with a thickness of 2 cm. The bulk and shear dry frame moduli K_m and μ_m of the DZ correspond to the arithmetic mean values of the material properties for the fracture and the intact background. The porosity ϕ, and the permeability k, are higher than those for the background and chosen to enhance the effects associated with FPD between the fracture and DZ at sonic frequencies.

Figure 2 shows the P-wave velocity of the background for the above three scenarios calculated using Gassmann's (1951) equations. For the stochastically heterogeneous case (Figure 2b), we consider one realization containing a fracture and six independent realizations of the heterogeneous background for the estimation of the reference signal through averaging. The number of independent realizations to determine the reference signal represents a trade-off between the computational cost and the number of traces expected to be representative of an intact formation in field applications. Please note that in Figure 2c, a different color scale is used for the model containing the DZ to enhance its visibility.

3.2. Extraction of the Critically Refracted P-Wave

Figures 3a–3c show the synthetic seismograms for a homogenous background without and with a horizontal fracture, and the corresponding difference between the two data sets, respectively. As expected for the considered crystalline-type environment, critically refracted P- and S-waves, pseudo-Rayleigh, and Stoneley waves are visible in the synthetic source gathers. These wave modes interact with the fracture. The wavefield in the vicinity of the fracture is additionally complicated due to reflected P-waves as well as tube waves originating from the fracture. Given that only the refracted P-wave is used for fracture compliance estimation, a tapered time window denoted by the black rectangle is utilized to isolate it. Here, a cosine window is centered around the maximum amplitude of the first-arriving wave cycle. The length of the time window influences the behavior of the group and phase time delay and, consequently, the compliance estimates. Previous work

Figure 1. Comparison of histographic distributions of P-wave velocity for the numerical model with a heterogeneous background (light brown) and the observed P-wave velocity of the full-waveform sonic data considered in Section 4 (blue).
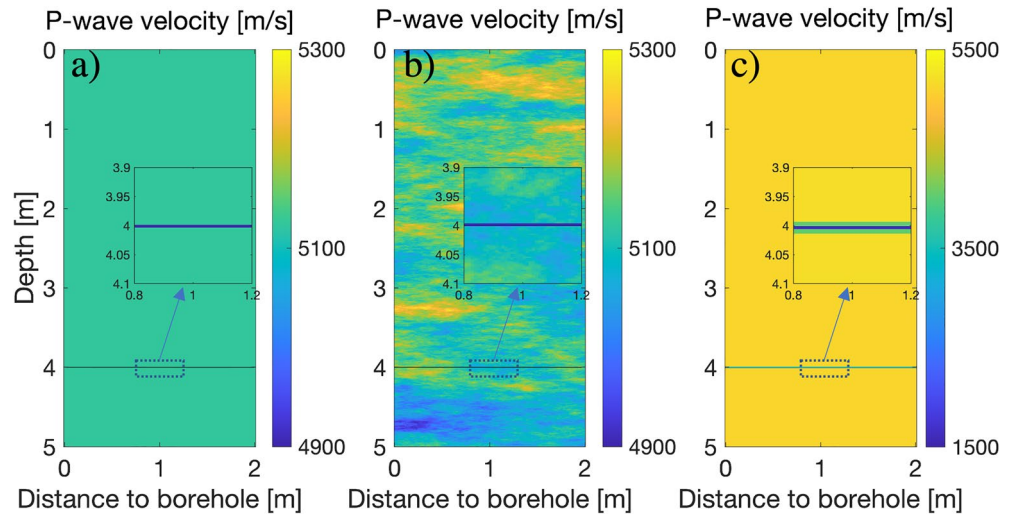
Figure 2. Distribution of P-wave velocity for (a) a homogeneous background, (b) a stochastically heterogeneous background, and (c) a DZ embedded in a homogeneous background. The horizontal fracture, whose structure is illustrated by blowups, is located at 4.0 m depth.

has shown that the phase time delay is not as sensitive as the group time delay to the time window length (Möllhoff & Bean, 2009). This is mainly because a relatively narrow time window does not contain all the information associated with the group velocity. For the synthetic study, we found that the optimal length of the time window is 0.1 ms, which approximately corresponds to twice the dominant time period of the source signal. This window length is used for all synthetic data considered.

Figure 4 shows comparisons for the extracted refracted P-waves of the three scenarios considered: (a) homogeneous background with and without a fracture (Figure 4a); (b) stochastically heterogeneous background with and without a fracture (Figure 4b); and (c) a homogeneous background with and without a fracture and associated DZ (Figure 4c). Note that for all scenarios, the refracted P-waves in the fractured models (red traces) after the fracture (around trace 20) exhibit lower amplitudes and later arrival times compared to the intact case without a fracture (black traces). The high amplitudes in the immediate vicinity of the fracture observed for all scenarios are related to the interference between the refracted P-wave and the tube wave generated by the hydraulically open fracture, which evidently affects compliance estimates from the corresponding receivers. Figure 4a presents the ideal scenario of a homogeneous background, for which we observe the expected consistency of P-wave arrival times and amplitudes between the intact and fractured cases for receivers located before the fracture. For the stochastically heterogeneous background (Figure 4b), the black traces correspond to the averaged reference traces
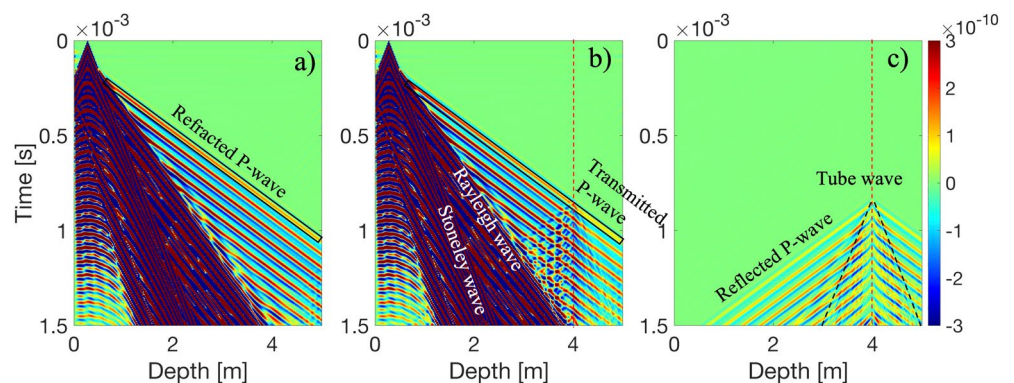
Figure 3. Synthetic seismograms recorded at the center of the water-filled borehole for a homogeneous background (a) without and (b) with a horizontal fracture denoted by the red dashed line at 4 m depth, and (c) corresponding difference. The black rectangle enclosing the first arrivals denotes the time window used to extract the critically refracted P-wave.
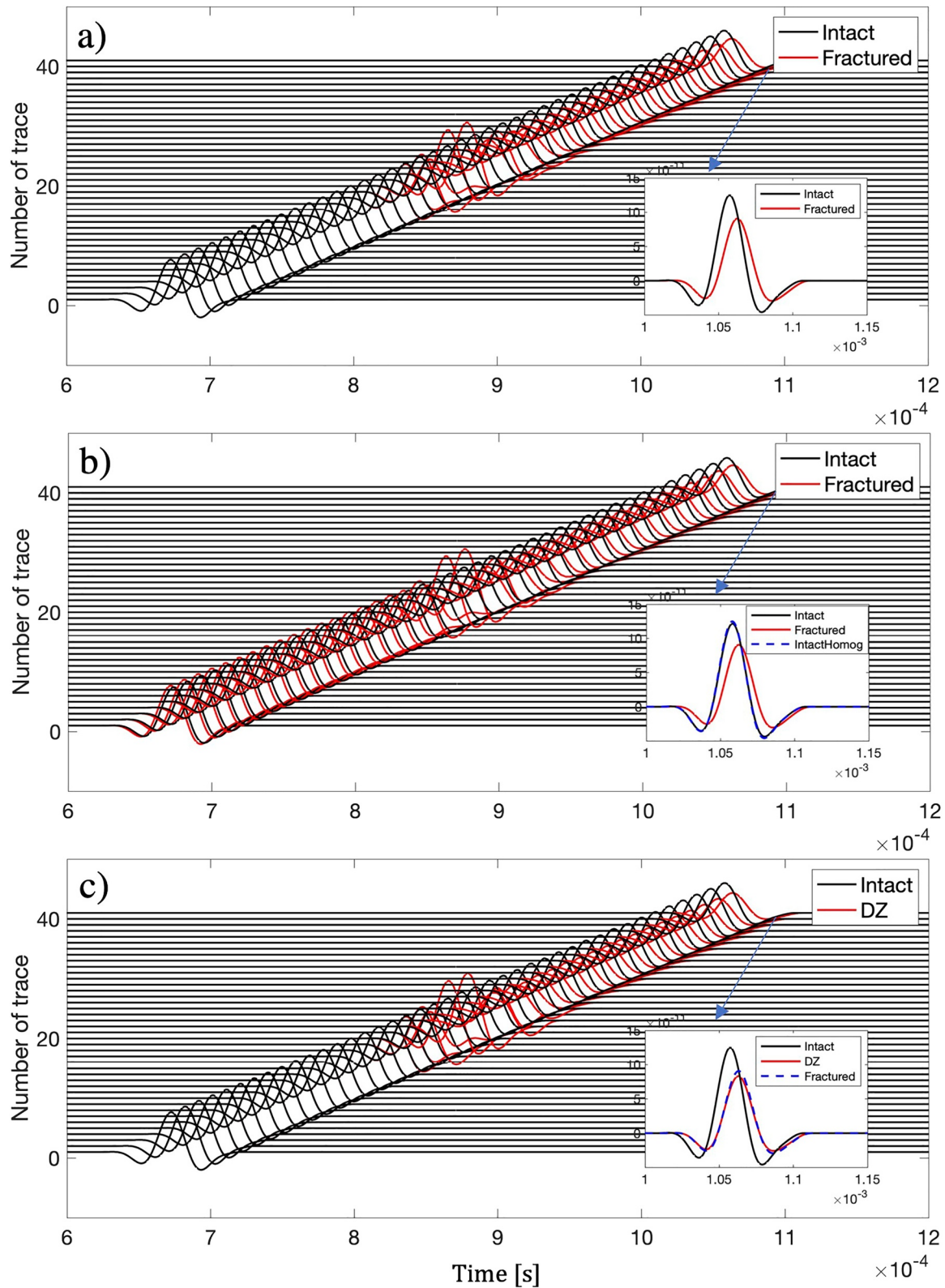
Figure 4. Refracted P-waves extracted from synthetic data for (a) homogeneous background, (b) heterogeneous background, and (c) a fracture with a DZ in a homogeneous background. The inserts show the refracted P-wave arrival for trace 41. Please note that the blue dashed curves in the inserts of (b and c) correspond to the P-waves for the intact and fractured scenarios shown in the insert of (a).

for six independent model realizations. Some discrepancies in the amplitudes and travel times can be observed between the intact and fractured rock even for receivers before the embedded fracture due to the variability of the background P-wave velocity. The characteristic scale of the background heterogeneity in the direction of wave propagation is comparable to the dominant wavelength of the refracted P-wave, which together with the average path length points to the potential presence of scattering (Aki & Richards, 1980). The insert in Figure 4b additionally shows the refracted P-wave for the intact homogeneous model (blue trace). This waveform and the one of averaged reference trace are quite similar, thus, indicating that the effect of the background heterogeneity on the averaged reference trace is rather small. Furthermore, there is no clear evidence of scattering effects in the averaged trace either. Figure 4c shows the refracted P-waves for the model containing a fracture with a DZ. The insert demonstrates that the presence of the DZ increases the amplitude decay and phase delay with respect to the same fractured model without DZ.

3.3. Fracture Compliance Estimation

To compute the spectral quantities involved in Equations 2, 6 and 7, we apply the Fourier transform to the extracted refracted P-waves shown in Figure 4, from which we obtain the fracture-induced phase shift $\delta\theta$ as well as the amplitude ratio $A^{\text{int}}/A^{\text{fra}}$ at the nominal source frequency of 20 kHz (e.g., Molyneux & Schmitt, 2000). The phase and group time delays are evaluated using Equations 4 and 5. For the stochastically heterogeneous model, the mean value of impedance is chosen for the background rock. This is justified since the range of impedance values for the considered model has a negligible impact on the compliance estimate as illustrated in Appendix B. The first, second, and third rows of Figure 5 correspond to the fracture-induced time delays, amplitude ratios, and compliance estimates from the three methodologies, respectively. Note that the group time delay as predicted by the linear slip model (Equation 4) exhibits a theoretical maximum depending on the frequency and compliance of a considered scenario. We found that this theoretical limit is breached for the estimates in Figures 5a and 5c, which implies that the assumptions of the linear slip model are not strictly valid anymore. The implications are further discussed in Appendix A. To assess the robustness of the compliance estimates, we compare them with the solution obtained using the poroelastic thin-layer model of Barbosa et al. (2016). This model allows to compute the P-wave reflection and transmission coefficients associated with a soft thin-layer emulating a fracture embedded in a homogeneous porous background. From the calculated transmission coefficient of a normally incident P-wave, the normal compliance is obtained using Equation 2. Compared to the classic definition of fracture compliance of Schoenberg (1980), that is, the ratio of the aperture and the undrained P-wave modulus, the poroelastic thin-layer model takes additional fractured-related seismic wave propagation phenomena into account, notably scattering and FPD between the thin layer and its embedding background. For the fracture parameters listed in Table 1 and a frequency of 20 kHz, the complex-valued compliance is $Z_{tl}^5 = 9.93. \times 10^{-13} - i \cdot 4.65 \times 10^{-14}$ m/Pa, where the superscript 5 refers to the fracture aperture in mm and the subscript tl refers to the thin-layer solution. Since the time delay methods are not strictly valid in the case of complex-valued fracture compliance, we shall first focus on the real component of the compliance estimates.

The left, middle, and right panels of Figure 5 correspond to the results for the three considered scenarios. The real component of compliance for the thin-layer solution is indicated by a dashed black line in the third row. For all the subfigures, each data point denotes one receiver offset or, equivalently, one trace beyond the fracture in Figure 4. The fracture location is denoted by a red vertical dashed line. In all cases, both the time delay and amplitude ratio are erratic in the vicinity of the fracture due to interference effects with other wave modes mentioned in the previous section. For the ideal homogeneous reference model, left column of Figure 5, phase (red dots) and group (blue dots) time delays, as well as the amplitude ratios, start to stabilize at a distance of 0.4 m from the embedded fracture and, hence, the compliance estimates become reliable for those receivers. The range of the interference zone denoted by the gray rectangle approximately equals 1.5 times the dominant wavelength, which is consistent with the observation of Barbosa et al. (2021). Figure 5g shows the compliance estimates inferred by the three methods. The relative differences between the averaged estimates for receivers after the interference zone and the thin-layer solution for the transmission (red), phase (green), and group (blue) delay schemes are 2.7%, 2.1%, and 10.0%, respectively. Thus, for this ideally homogeneous background, both the transmission and time delay methods produce adequate compliance estimates even in the theoretical limit of applicability of the linear slip model (Appendix A).
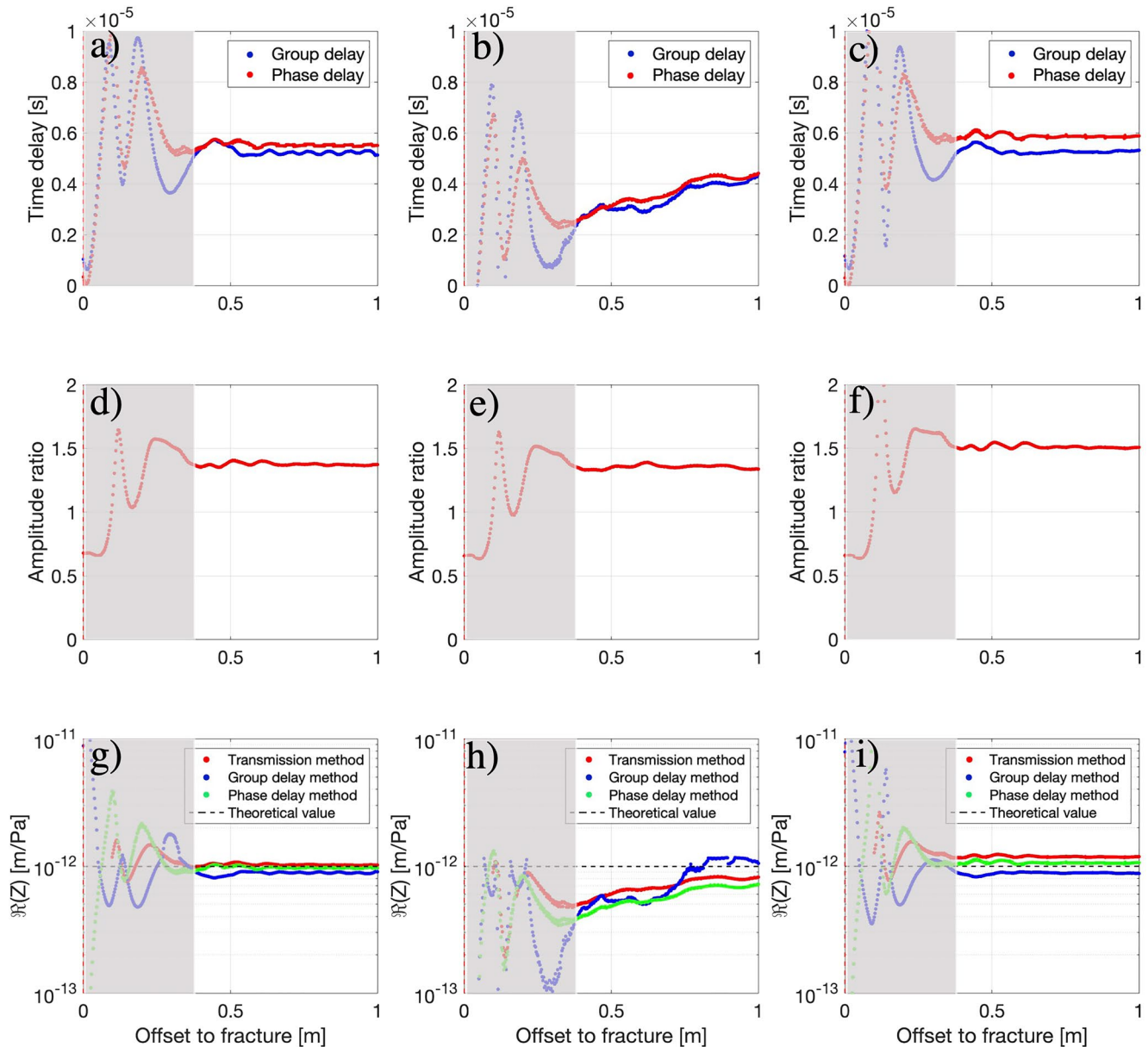
Figure 5. (a–c) Fracture-induced time delay, (d–f) amplitude ratio, and (g–i) compliance estimates for the homogeneous background (left column), stochastically heterogeneous background (middle column), and a DZ in homogeneous background (right column). Red and blue dots for the first row denote the phase and group time delays, respectively. Red, green, and blue dots in the third row correspond to the compliance estimates inferred by the transmission, phase, and group delay methods, respectively. The real component of the fracture compliance for the thin-layer model is illustrated by the black dashed horizontal line. The red dashed vertical line and gray rectangle for all subfigures denote the fracture location and associated interference zone, respectively.

For the stochastically heterogeneous model, after the gray-colored interference zone, both the group and phase time delays (Figure 5b) show smaller time delays than that of the homogeneous case. A closer inspection of the averaged reference trace reveals that its underlying propagation velocity is slower compared to the single realization of the heterogeneous model before the embedded fracture. This results in a systematic underestimation of the compliance (Figure 5h). Figure 5e shows that the amplitude ratio A^{int}/A^{fra} for the stochastically heterogeneous background model is similar to the one of the homogeneous scenario, thus, indicating that scattering does not play a significant role. Furthermore, a trend of increasing time delays with increasing distance from the fracture can be observed. This trend is attributed to the local velocity fluctuations in the vicinity of the fracture. In Figure 2b, a zone with lower velocities can be observed approximately 0.2 m below the fracture. Such a low-velocity zone will start to contribute to the time delays with increasing offset from the fracture. This, in turn, explains the apparent
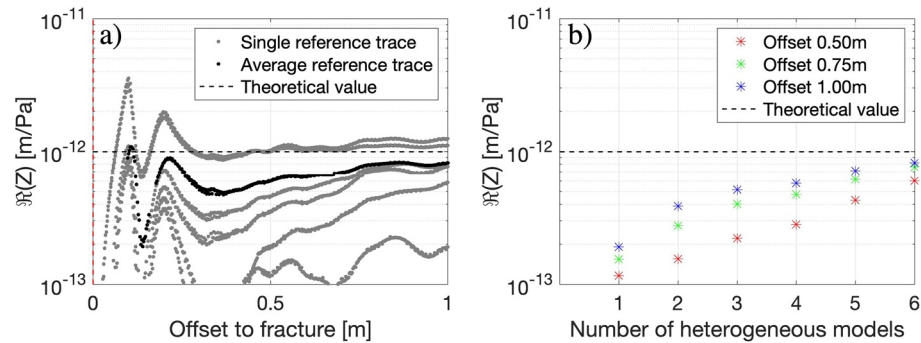
Figure 6. (a) Fracture compliance estimates using the phase delay method for six reference traces corresponding to the realizations of the heterogeneous background model (gray) and for the averaged reference trace (black). (b) Fracture compliance for three offsets as a function of the number of heterogeneous model simulations used to build the reference signal. Red, green, and blue asterisks correspond to estimates at 0.5, 0.75, and 1.0 m offsets from the fracture, respectively.

trend of increasing time delays. The compliance estimates shown in Figure 5h exhibit the same trend as those for the time delays. Overall, the transmission method produces the most reliable estimates with a relative difference of 26.5% to the thin-layer model, whereas the estimates for the phase time delay methods exhibit differences of ~30%. The comparison shown in Figure 5h indicates that these techniques provide more stable results than the group time delay method. Compared to the homogeneous case, the discrepancy between the thin-layer model and estimated compliance increases for all three methods. Nevertheless, the compliance estimates inferred by the three methods are still reasonable in the presence of strong local heterogeneities.

To further explore the impact of a stochastically heterogeneous background on the reference trace, we estimate the fracture compliance for the homogeneous fracture model using six different reference traces obtained from each of the six heterogeneous models. In this case, the differences in the compliance estimates can be attributed solely to the choice of the reference trace. For simplicity, only the results for the phase time delay method are shown in Figure 6a. The results for the other two methods show similar trends. Due to the strong heterogeneity of the stochastic models, the estimated fracture compliances differ up to approximately one order-of-magnitude depending on the chosen reference trace. The black curve in Figure 6a shows the compliance estimate for the average of the six reference traces. Compliance estimates for the averaged reference are close to the thin-layer solution. Figure 6b shows the evolution of fracture compliance for three receivers with offsets to the fracture equal to 0.5, 0.75, and 1.0 m, with the number of traces averaged to obtain the reference trace. The consistent behavior for the three receivers illustrates that heterogeneity effects can be effectively averaged out to get reasonable compliance estimates and that considering more than six traces tends to be sufficient for the chosen example to get a relative difference similar to the homogeneous background case (Figure 5g). Nevertheless, this numerical example highlights the significant uncertainty in fracture compliance estimation that can be associated with the reference signal if it is not carefully chosen.

For the scenario with a DZ, the difference in the first arrival times, which is not directly obvious in the insert of Figure 4c, is revealed. Figure 5c shows that the presence of a DZ leads to slightly larger phase delays than the first homogeneous scenario (Figure 5a). Additionally, Figure 5f illustrates that the DZ also results in additional amplitude decay, as expected from the observations in the insert of Figure 4c. The increases in the amplitude decay and time delay are mostly related to (a) an increase in hydraulic communication between the embedded fracture and permeable DZ, which promotes FPD at the considered sonic frequency, and to (b) the larger effective width of the fracture due to the presence of the mechanically weak DZ. For the first potential factor, previous studies have shown that the hydraulic communication in response to FPD between the fluid-saturated fractures and permeable host rock increases the real component of fracture compliance by reducing the stiffening effect of the saturating fluid within the fracture (Barbosa et al., 2016; Caspari et al., 2019; Rubino et al., 2015; Sotelo et al., 2021). The second factor is related to the finite width of the DZ and fracture, which, at the relatively high frequencies considered here, may result in scattering of waves inside the fracture and/or the DZ (Nakagawa & Schoenberg, 2007; Sotelo et al., 2021).
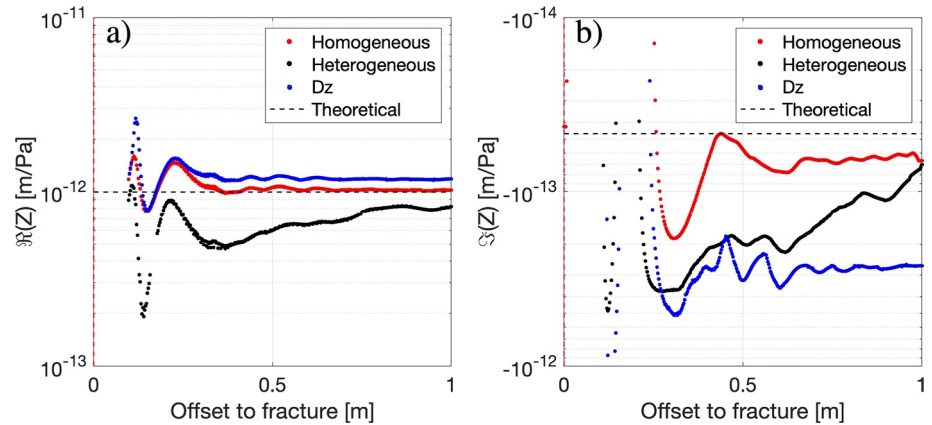
Figure 7. (a) Real and (b) imaginary components of the complex-valued compliance by the transmission method for three numerical models and the thin-layer model (black dashed line). Red, black, and blue dots correspond to the estimates for the homogeneous, stochastically heterogeneous, and DZ models, respectively. The red dashed vertical lines denote the fracture location.

Figure 5i shows that the transmission and phase delay methods are sensitive to the effects associated with the presence of a DZ and provide higher effective compliance estimates compared to the estimates in Figure 5g. We also observe a larger relative difference between the compliance estimates from transmission and phase delay methods with respect to the results in Figure 5g. This is related to the fact that the transmission method can account for the viscoelastic nature of the fracture that is not explicitly taken into account by the time delay methods. The imaginary component of the fracture compliance quantifies energy dissipation prevailing at the fracture and contributes to the transmission losses across the fracture. Figure 7 shows the real (a) and imaginary (b) components of the complex-valued compliance estimated by the transmission scheme for the three scenarios considered in the numerical tests. The compliance of the thin-layer model is denoted by the horizontal black line. Compared to the fracture compliance Z_{tl}^5, the real component inferred from the transmission method is overestimated for the homogeneous and DZ models and underestimated for the stochastically heterogeneous scenario, whereas the magnitude of the imaginary component is always overestimated. As the imaginary component quantifies energy dissipation across the fracture, the values shown in Figure 7b are positively correlated with the amplitude ratios shown in Figure 5. The averaged imaginary components for the homogeneous (red) and stochastically heterogeneous (black) cases for receivers from 0.5 to 1.0 m offset are -7.5×10^{-14} m/Pa and -9.8×10^{-14} m/Pa, respectively, and thus comparable to the thin-layer model (-4.65×10^{-14} m/Pa). For the DZ model (blue), the averaged imaginary component of the compliance estimate (-2.8×10^{-13} m/Pa) is roughly one order-of-magnitude larger than that for the thin-layer solution due to the combined effects of enhanced FPD and scattering effects. As a result of the increased imaginary component, the relative difference of the real-valued compliance estimates from the phase time delay increases from 4.9% (Figure 5g) to 10.3% concerning the transmission method (Figure 5i).

It is important to mention that the performance of time delay methods in the case of a fracture surrounded by a DZ represents a worst-case scenario due to the combined effect of the fracture scattering and the enhanced FPD on the transmission of the seismic waves. Figure 8 illustrates the expected impact due to only scattering of waves inside the fracture by changing the mechanical aperture of a fracture without DZ. We compare compliance estimates for a fracture with apertures of 1 mm (Figures 8a and 8b), and the previously considered 5 mm (Figures 8c and 8d), embedded in the same homogeneous background. A larger fracture aperture results in an increased time delay and amplitude decay, which translates into a larger compliance for the fracture with an aperture of 5 mm ($9.93. \times 10^{-13} - i \cdot 4.65 \times 10^{-14}$ m/Pa) compared to the one with an aperture of 1 mm ($2.20 \times 10^{-13} - i \cdot 1.79 \times 10^{-14}$ m/Pa). The impact of scattering associated with the finite aperture of the fracture on compliance estimation can also be observed in the increased imaginary component in the 5 mm case compared to the 1 mm case. In spite of this, the relative difference of the real component of compliance between the transmission and the phase time delay methods for the 5 mm scenario (4.9%) is significantly smaller than the corresponding discrepancy in the case of the presence of a DZ (10.3%).
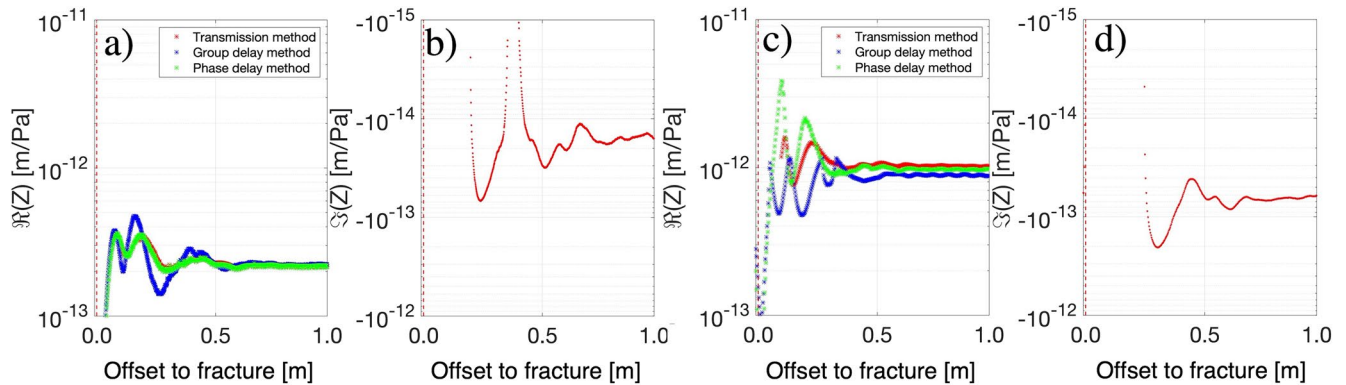
Figure 8. Fracture compliance estimates for fracture apertures of (a and b) 1 mm and (c and d) 5 mm. Red, blue, and green dots in (a and c) correspond to the real-valued compliance inferred by the transmission, group delay, and phase delay methods, respectively. The imaginary component of compliance shown in (b and d) can only be estimated by the transmission method. Red vertical lines denote the fracture location.

Overall, the numerical tests performed in this section allow us to conclude that the transmission method and time delay methods are, in general, capable of providing adequate compliance estimates both in the presence of strong background heterogeneity and in the presence of a DZ surrounding the fracture. Our results also show that the considered time delay methods, especially the phase time delay scheme, are reliable even in the presence of additional energy dissipation in the fracture due to enhanced scattering and/or FPD effects, in which case the fracture compliance becomes complex-valued. Arguably most importantly, the results illustrate that, in the presence of background heterogeneity, the choice of the reference signal is indeed an important source of uncertainty for the estimation of fracture compliance from FWS data, which merits particular attention and care. We found that, in the case of stochastically heterogeneous media, a relatively small number of traces are necessary to average out background heterogeneity-related effects and obtain satisfactory compliance estimates. In the next section, we will apply the transmission and phase time delay methods to the standard, production-type FWS data collected in granitic rocks. The group delay method is not considered anymore since it is ambiguous with its two possible solutions and it is less reliable than the phase delay method.

4. Application to Observed FWS Data

4.1. Experimental Setting

In the following, we seek to assess the applicability of the transmission and phase delay methods for standard FWS data acquired along a borehole at the Bedretto Underground Laboratory for Geosciences and Geoenergy. The Bedretto Lab is located ~2 km from the entrance of a 5.2-km-long abandoned tunnel traversing the crystalline rocks of the so-called Rotondo Granite in the central Swiss Alps (Gischig et al., 2020; Hertrich et al., 2021). The considered borehole, referred to as SB1.1, is 28.6 m deep and penetrates several pre-existing natural fractures, which have been identified by acoustic televiewer (ATV) logging. The selected borehole was used for a hydraulic stimulation experiment to characterize the in situ stress by measuring the formation breakdown, fracture closure, and fracture reopening pressures (Bröker & Ma, 2022). This resulted in the creation of several new small fractures. Two independent FWS data sets, which comprise repeated logging runs before and after the mini hydraulic stimulation, referred to as pre- and post-stimulation data sets, were collected. This permits to test the methods for natural and newly generated fractures, as well as to assess the repeatability of estimates by comparing compliance of a pre-existing natural fracture outside the stimulated zone for two independent logging runs.

A MSI 2SAA-1000-F modular multi-frequency sonic logging tool was employed to collect FWS data along SB1.1 before and after the hydraulic fracturing campaign at a nominal source frequency of 20 kHz. The tool contains a transmitter at its lower end and five receivers spaced at 0.305 m (1 ft) intervals, with the first receiver being located 0.915 m (3 ft) above the transmitter. Logging was carried out in a standard, production-type manner by moving the sonic logging tool from the bottom to the top of the borehole with a constant speed of 1 m/min while "shooting" every 2 cm. The acquisition parameters are summarized in Table 2. Compared to static FWS data as in Barbosa et al. (2021), the friction between the moving centralizer and the borehole wall reduces the

Table 2
Full-Waveform Sonic Acquisition Parameters for Borehole SB 1.1

Source depth range (m)	3.06–28.62
Spatial sampling rate (m)	0.02
Time sampling rate (us)	4
Recording time (us)	1,324
Nominal source frequency (kHz)	20
Number of stacks	4

S/N ratio. To assess the S/N ratio for the refracted P-waves, we extract the P-waves by a tapered time window of 0.1125 ms length, with the center of the window coinciding with the maximum amplitude of the first cycle of the refracted P-wave. The noise level is estimated from the recorded noise before the first recorded signal in a time window of the same length. The S/N ratio is obtained as the ratio between the rms amplitudes of the refracted P-wave signal (S) and the noise signal (N). Figure 9 shows S/N for all five receivers. A low S/N of around five or less for the two far-offset receivers can be observed, which is not sufficient for a reliable estimation of small time delays. This criterion is based on a numerical test, in which the simulated P-waves are contaminated by the noise extracted from the observed FWS data before the first arrivals. Evaluating the compliance using the transmission method, we observe that the error between the theoretical and estimated compliance becomes significant for S/N < 5. Consequently, only the traces from the first three receivers closest to the transmitter (i.e., Rx1, Rx2, and Rx3) and with S/N larger than 5 are considered for fracture compliance estimation.

4.2. Database

To test the compliance estimation methods, we select a pre-existing isolated natural fracture, which is not directly affected by the hydraulic stimulation experiment, and a new fracture generated during the hydraulic fracturing experiment. Figure 10a shows the FWS recording for the first receiver Rx1 after stimulation. The pre-existing natural fractures intersected by SB1.1 are denoted by the red dashed vertical lines, while the newly generated ones correspond to black dashed lines. An isolated pre-existing fracture located at 19.2 m depth, denoted as N1, can be observed on the pre-stimulation ATV log (Figure 10b). The post-stimulation ATV log of SB1.1 (Figure 10c) shows two new fractures, denoted as F1 and F2, at depths of 14.45 and 17.36 m, respectively, as well as two new fractures, denoted as F3 and F4, at depths of 19.68 and 19.86 m, respectively. To illustrate the impact of the new fractures on the refracted P-waves, we also plot the first arrival times for the pre- and post-stimulation FWS data, denoted by the red and blue curves in Figure 10a. The first arrivals, corresponding to the maximum amplitudes of the first cycle of the refracted P-wave, are manually picked. Good agreement between the two sets of first arrivals can be observed except for signals propagating across the new fractures F1 and F2, around which later arrival times for the post-stimulation data occur. A similar observation can also be made for the other two new fractures F3 and F4. The general trend of the first arrivals in the vicinity of the pre-existing fracture N1 does not seem to be severely affected. Thus, a comparison between compliance estimates for fracture N1 from two independent data sets will permit us to assess the repeatability/reliability of the estimates. Since F3 and F4 show very small time delays and F2 is steeply dipping, we analyze fracture F1 as an example of a man-made fracture, as it is quasi-normal to the borehole axis and rather isolated.

4.3. Selection of the Reference Signal

As illustrated by our synthetic study, a careful selection of a representative reference signal from the intact sections of borehole SB1.1 is essential for a reliable estimation of fracture compliance. To minimize the impact of
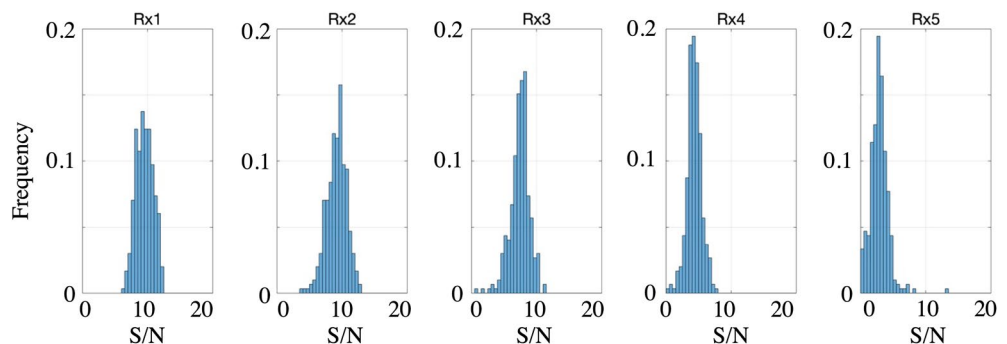
Figure 9. S/N of the refracted P-wave for receivers Rx1 to Rx5 for the pre-stimulation full-waveform sonic data.
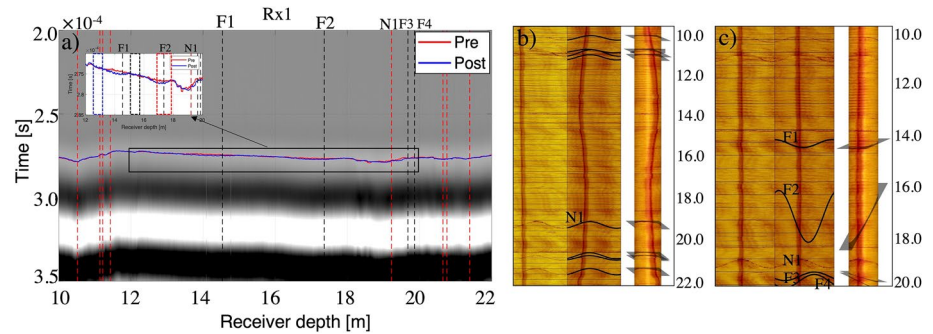
Figure 10. (a) Full-waveform sonic data for the first receiver Rx1 in borehole SB1.1 after hydraulic stimulation. The red and black vertical dashed lines correspond to the natural and newly generated fractures, respectively. The red and blue curves indicate the first arrivals of the refracted P-wave for the pre- and post-stimulation data, respectively. The insert corresponding to the black rectangle shows a zoom of the first arrivals and the location of the reference intervals. (b) Pre- and (c) post-stimulation ATV logs with the pre-existing and new fractures.

local variability of the background properties, we seek representative intervals of intact rock. The reference signal is then determined by averaging all recorded signals in the chosen interval, whereby traces with S/N lower than 5 are not considered. Figure 10b shows that an extended intact section exists above N1 prior to hydraulic stimulation. However, the first arrival times, presented in the insert of Figure 10a, reveal a trend of decreasing velocity toward the fractured zone at the bottom of the borehole. For this reason, we must choose an intact section as close as possible to fracture N1. The zone with relatively flat first arrivals between 16.9 and 17.9 m in receiver depth, or, equivalently, between 17.8 and 18.8 m in source depth, shown by the red dashed rectangle in Figure 10a, is selected for the estimation of the reference signal and denoted as RF1. However, this reference interval cannot be utilized for the post-stimulation compliance estimate of N1, since this zone now hosts the newly generated fracture F2. Due to the steep dip of fracture F2, a second intact section between 15.1 and 15.6 m receiver depth (16.0–16.5 m source depth), shown by the black dashed rectangle in Figure 10a, is used as reference signal RF2, which will be used to compare the pre- and post-stimulation compliance estimates of N1. The repeatability of the estimates can be assessed by comparing the results for N1 when using the reference traces RF1 and RF2. For the newly generated fracture F1, the trend of increasing arrival times, indicative of decreasing velocity with depth, is also an issue for the choice of the reference section. To minimize the impact of this trend on the compliance estimation, we consider two intact sections in the vicinity of fracture F1 to compute the reference signals. One is above fracture F1 from 12.8 to 13.3 m receiver depth (13.7–14.2 m source depth) denoted by the blue dashed rectangle in Figure 10a, and the other one is the previously defined section for RF2, which is located below F1. To obtain a representative reference signal for F1, the traces associated with these two reference intervals are averaged to obtain a single reference trace RF3. Finally, we consider a fourth reference signal RF4 to compute the compliance of F1 using the traces from 13.1 to 15.1 m receiver depth of the pre-stimulation FWS data. This is a practically interesting scenario as it assesses the potential of combining pre- and post-stimulation data, making use of the actual intact section surrounding newly created fractures.

4.4. Estimation of Fracture Compliance

Based on the results from the numerical study, traces located closer than 1.5 times the dominant P-wave wavelength to the fractures are not considered for fracture compliance estimation. For the required impedance of the background rock in the estimation, and based on the analysis shown in Appendix B, the mean P-wave velocity of the sonic log is taken, and for the density, we use the saturated bulk density measured on core samples in the laboratory (David et al., 2020). Figure 11 shows the results for N1 using the reference trace RF1 and the pre-stimulation data. Figures 11a–11d correspond to the fracture-induced phase time delays, amplitude decay, and compliance estimates inferred by the transmission and phase delay methods, respectively. Here, we take advantage of having multiple receiver positions for the same source-receiver offset and illustrate the fracture compliance as a function of receiver depths. The redundancy of information given by multiple shot positions, a relatively small spatial sampling, and the three receivers allows us to get robust compliance estimates. In principle, for a single fracture in a homogeneous formation, the estimates obtained from the three receivers are expected
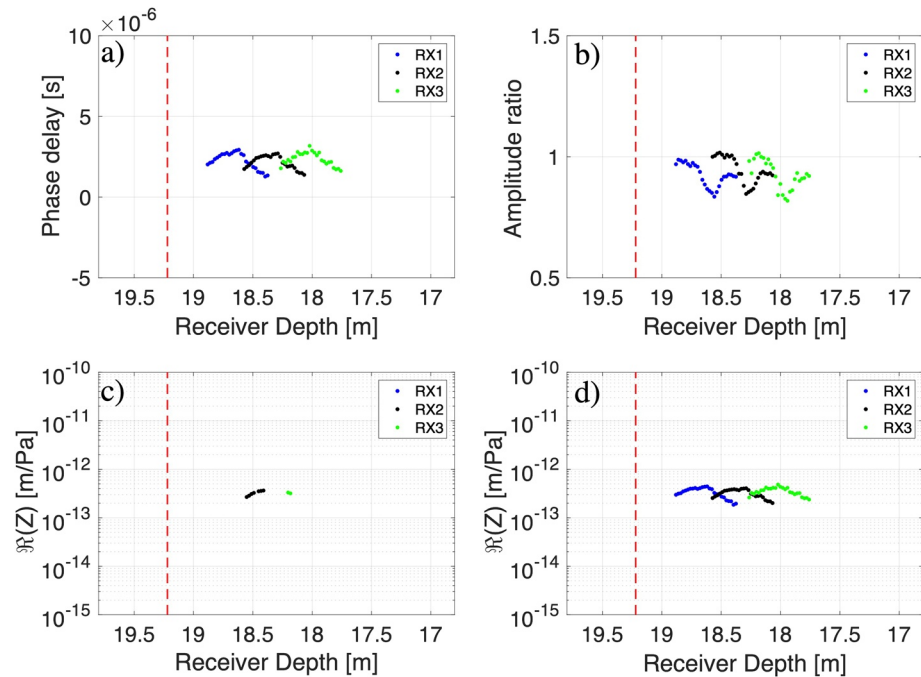
Figure 11. Fracture-induced (a) phase time delay, (b) amplitude ratio, and compliance estimates inferred using (c) the transmission method and (d) the phase time delay method, respectively, for fracture N1 at the nominal source frequency of 20 kHz for the pre-stimulation data. For all subfigures, blue, black, and green dots denote the locations of three receivers. The vertical red dashed lines denote the location of fracture N1.

to be offset-independent. While Figure 11a shows that the phase time delays are similar for the three receivers, they vary with the source position. As expected, the consistent pattern as a function of the receiver position is replicated by the compliance estimates in Figure 11d. This pattern cannot be explained by noise, as, in this case, we would expect more erratic estimates. Based on the analysis of Figure 5h, the compliance variation is related to the presence of heterogeneity in the vicinity of the fracture.

The mean normal compliance estimates of N1 for the transmission method and the phase delay methods are 3.5×10^{-13} m/Pa and 3.3×10^{-13} m/Pa, respectively. Their similarity confirms the conclusions from the numerical tests that both methods are in principle comparable for fracture compliance estimation. Figure 11b presents the amplitude ratio $A^{\mathrm{int}}/A^{\mathrm{fra}}$ at the nominal source frequency, which is only utilized in the transmission method. According to the linear slip model, the amplitude ratio for the three receivers at the chosen depth range should be larger than 1. However, this is not the case for most of the signals. Thus, only a few viable traces with $A^{\mathrm{int}}/A^{\mathrm{fra}} > 1$ can be utilized to compute the compliance with the transmission method (Figure 11c). To explore the reasons for the low amplitude ratios observed in Figure 11b, we show the depth dependence of the spectral amplitudes of the refracted P-wave at 20 kHz for the pre-and post-stimulation FWS data (Figure 12). For 14–18 m receiver depth, the amplitudes generally exhibit an ascending trend towards the fractured zone. The relatively high amplitudes and their strong variability around N1 compared with the reference interval for RF1 denoted by the red rectangle results in amplitude ratios lower than 1. This makes the use of the transmission method impracticable. Thus, in the following, we only focus on the phase time delay method, which is most suitable for the data sets at hand.
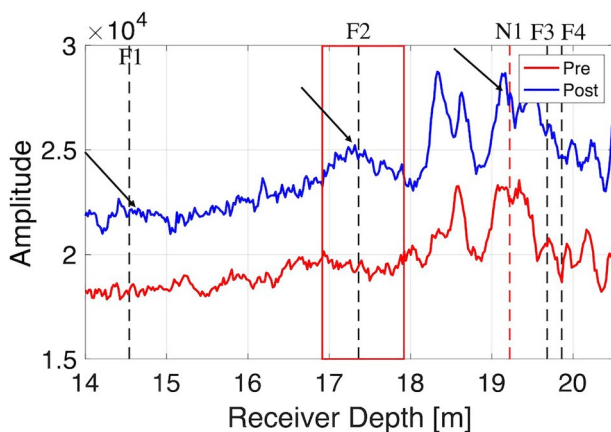
Figure 12. Spectral amplitudes for refracted P-wave at 20 kHz for the pre-(red) and post-(blue) stimulation full-waveform sonic data sets. The red and black vertical dashed lines denote the locations of the natural and new fractures, respectively. The red rectangle denotes the range of RF1.

Figure 13 shows the results for the natural fracture N1 using the two reference traces RF1 and RF2 from the pre-stimulation FWS data as well as RF2 from
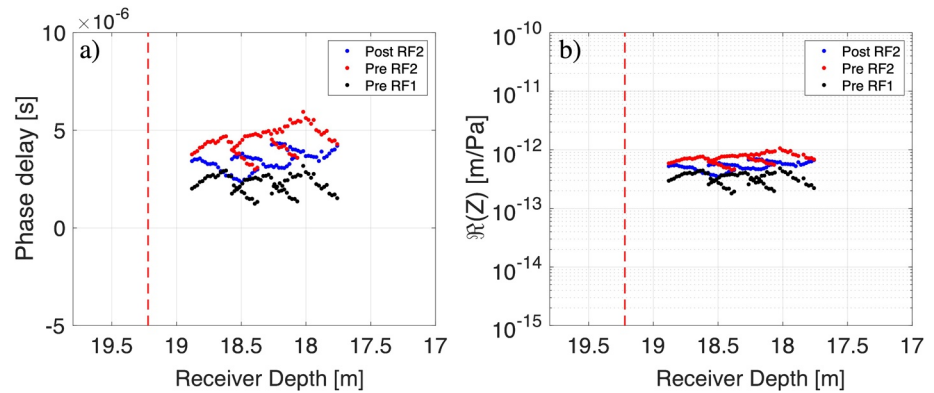
Figure 13. (a) Phase time delay and (b) compliance estimates for N1 at the nominal source frequency of 20 kHz. The blue and red dots correspond to the results using the reference interval RF2 for the post- and pre-stimulation data, respectively. The black dots illustrate the results shown in Figure 11d using RF1 and pre-stimulation data. The red dashed lines denote the location of fracture N1.

the post-stimulation data. For RF2, the phase time delays (Figure 13a) show the discrepancy between the pre- and post-stimulation FWS data. These differences in the time delays are also reflected in the pre- and post-stimulation mean compliance estimates, which are 6.5×10^{-13} m/Pa and 4.5×10^{-13} m/Pa, respectively. Since the first arrival times from pre- and post-stimulation data in the reference section of RF2 (black dashed rectangle in insert of Figure 10a) are in good agreement, the observed differences in the phase time delay and fracture compliance are most likely due to changes in the vicinity of fracture N1. In particular, the hydraulic stimulation that produced fractures F3 and F4 may have affected the host rock in the vicinity of N1. Next, we assess the impact of the general velocity trend in the borehole by considering the reference signals RF1 and RF2 and the pre-stimulation data. Figure 13a shows that the phase time delays for RF2 (red) are approximately two times larger than their counterparts for RF1 (black). This discrepancy is mainly due to the fact that RF2 exhibits faster arrival times or, equivalently, higher velocities than RF1 as can be observed in Figure 10a. Consequently, the mean compliance estimates are 6.5×10^{-13} m/Pa and 3.3×10^{-13} m/Pa using RF2 and RF1, respectively. Given that fracture compliance estimates tend to be order-of-magnitude-type measurements, these values can nevertheless still be regarded as being mutually consistent.

Finally, we proceed to estimate the compliance of the new fracture F1 generated during the hydraulic stimulation experiment. Figure 14 presents the results at the nominal source frequency of 20 kHz using the reference traces RF3 (post-stimulation data) and RF4 (pre-stimulation data). Given that the time delays produced by the new fracture F1 (Figure 14a) are notably smaller than those related to N1 (e.g., Figure 11a), the former is more affected by noise. As the transmitter approaches the fracture, the time delays start to decrease and become eventually negative, which is caused by the predominance of the velocity trend of the background rock over the time delay caused
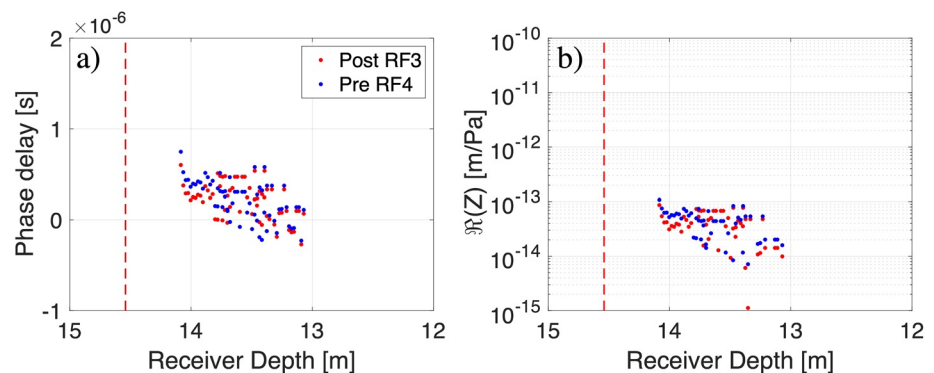
Figure 14. (a) Fracture-induced phase time delay and (b) compliance for fracture F1 at the nominal source frequency of 20 kHz for post-stimulation data. Red and blue dots correspond to the reference RF3 for post-stimulation and using RF4 for pre-stimulation data, respectively. The red dashed lines denote the locations of the new fracture F1.

Table 3
Mean and Standard Deviation of Compliance Estimates for Fracture N1 and F1 for the Different Reference Traces

	N1			F1	
	Pre RF1	Pre RF2	Post RF2	Pre RF4	Post RF3
Mean (m/Pa)	3.3×10^{-13}	6.5×10^{-13}	4.5×10^{-13}	4.2×10^{-14}	4.1×10^{-14}
Standard deviation (m/Pa)	6.7×10^{-14}	1.2×10^{-13}	7.6×10^{-14}	2.7×10^{-14}	2.5×10^{-14}

by fracture F1. Hence, we only consider signals with positive time delays for fracture compliance estimation. The obtained average compliance value is similar for both reference signals, RF3 and RF4, with 4.2×10^{-14} m/Pa.

5. Discussion

The numerical tests and field data indicate that the largest sources of uncertainty for the estimation of fracture compliance from FWS data is associated with the choice of a representative reference signal in the presence of background heterogeneity. For the field data, the trend of the P-wave velocity provides the largest bias in the compliance estimates as illustrated by the mean estimates from the different reference intervals, which are summarized in Table 3. Table 3 also lists the corresponding standard deviation of the mean compliance estimates obtained from the redundancy of the measurements due to multiple shot points, the small sampling interval and three receivers. This provides a measure for the uncertainty of an estimate from a specific reference interval. For the natural fracture N1, the discrepancy between the mean compliance values for the two reference intervals RF1 and RF2 due to the velocity trend is clearly larger than the standard deviations for each of the intervals, which are roughly 5 times smaller than the mean values. The effect of the observed velocity trend becomes even more pronounced in the presence of small time-delays for the new, hydraulically generated fracture F1. To minimize this effect on the compliance estimation, the average of two reference sections, one above and another one below the fracture F1, was utilized. In the particular case of F1, it can be expected that estimates for a reference signal from an intact interval below this fracture would lead to negative time delays, while estimates from an interval above F1 would lead to too high compliance values. But even for the average of the two reference sections, the standard deviation is about half of the mean compliance, and thus the uncertainty for F1 is much higher than for N1. This high uncertainty of the estimate indicates the limitation of the phase time delay method in the presence of relatively small and stiff fractures, where the effects on wave propagation might become too small for robust estimates. Despite the relatively low compliance magnitude and the high uncertainty for the man-made fracture, the consistency of the results with those from the pre-stimulation data implies that the use of pre-stimulation data to define the reference signal to compute fracture compliance from post-stimulation data is a viable option to simplify the selection of the reference zone and minimize heterogeneity-related effects. Table 3 also illustrates that the mean compliance estimate for F1 is one order-of-magnitude lower than the one for the natural fracture N1. This result is expected since the hydraulic stimulation experiment was designed for stress testing creating only very small fractures compared to the pre-existing natural ones, which are related to pervasive brittle tectonic deformation during the late stages of the Alpine orogeny. This also agrees with their expressions in the ATV log, where N1 clearly exhibits a larger aperture than F1.

Compared with the compliance estimates for natural fractures from previous studies (e.g., Foord et al., 2015; Worthington & Lubbe, 2007), the estimate of N1 falls in the range of compliance estimates for fractures of the size of 1–10 m and is similar to the ones obtained from static measurements in a crystalline rock environment by Barbosa et al. (2021). It is expected that the natural open fractures created in response to regional-scale stress fields extend further from intersecting boreholes than man-made fractures from small scale hydraulic stimulation tests. However, it is to note that the fracture scale for F1 and N1 cannot be directly measured. Furthermore, we have conducted a series of numerical tests, in which we varied the fracture length from 0.25 to 2 m. The results indicate that as soon as the fracture length is larger than the width of the Fresnel zone, which is ∼0.7 m at 3.75 m distance from the source for the considered frequency, the impact on the estimated compliance becomes negligible. For the natural fracture N1 and man-made fracture F1, the width of the Fresnel zone for three receivers increases from ∼0.35 to ∼0.45 m. In all likelihood, this is smaller than their fracture length and, hence, the corresponding compliance is dominated by the aperture of the fracture. The impact of the fracture length on the compliance estimate is expected to depend on the geometry of the setup and frequency of the measurement,

which has to be considered for the development of scaling relationships. In this study, the fracture compliance is estimated for a single frequency, however, the method can be employed to obtain estimates at different frequencies within the sonic range. This, should, in principle, allow to capture effects associated with limited fracture lengths, which, in turn, is expected to be particularly relevant assessing the lengths of small induced fractures.

The fracture aperture is not only an important factor for the fracture compliance but also for the hydraulic properties of fractures. Although the hydraulic properties were not directly measured for the two fractures, their expression in the ATV log and their signatures in the FWS data provide some insights. From the ATV log, we observe that N1 exhibits clearly a larger aperture than the man-made fracture, and thus a larger hydraulic conductivity. This is supported by another wave phenomena, so called tube waves, which have been utilized to estimate hydraulic properties from VSP data (e.g., Bakku et al., 2013; Hunziker et al., 2020; Li et al., 1994). The larger the amplitude of the generated tube waves at the fracture opening intersecting the borehole, the larger is the hydraulic conductivity of the fracture. The magnitude of the tube wave amplitude can be inferred by the degree of wavefield interference in the first arrivals in the vicinity of the fracture. This can be observed in Figure 12 where the amplitude increase denoted by black arrows for the two man-made fractures F1 and F2 is clearly smaller than that for the natural fracture N1. Thus at least for the natural fracture, both the compliance estimate in the sonic range and hydraulic properties are most likely dominated by the aperture of the fracture. Although we observe clear differences in the compliance magnitude and their signature in the FWS data between the natural and man-made fractures, all these observations are related to some extent to the size of the fractures. An interesting additional parameter, which might reveal something more about the potential difference in the internal structure of man-made and natural fractures, might be the ratio of the normal to the shear compliance. Previous works have explored the impact of the saturating fluid as well as of geometric fracture characteristics, such as the roughness of the fracture walls and the number of contacts between the associated asperities on the normal-to-shear compliance ratio (e.g., Ahmadi et al., 2016; Lubbe et al., 2008). Since the saturation conditions of F1 and N1 can be regarded as equivalent, this ratio might provide interesting information regarding the detailed geometric characteristics of natural versus man-made fractures. The methodology considered in this study can be straightforwardly extended to shear compliance estimates, however, as opposed to the direct P-wave, the direct S-wave is more difficult to identify in FWS data and correspondingly uncertain to pick. While we plan to develop techniques for reliably estimating shear compliance in the future, the corresponding research is a technically challenging endeavor in its own right and, thus, beyond the scope of the current work.

6. Conclusions

In this work, we assessed the potential of inferring the compliance of individual fractures from standard, production-type FWS data in the presence of heterogeneity. To this end, we first considered a suite of canonical models and performed comparative tests on synthetic FWS data to evaluate the robustness of the transmission as well as group and phase time delays methods to estimate compliance of an individual fracture. The results indicate that all three methods produce adequate compliance estimates in the presence of strong heterogeneity. However, local velocity fluctuations influence the compliance estimates as indicated by the increase in compliance with offset for the synthetic data sets of the stochastic models. Satisfactory results in the numerical study were also obtained when the fracture is surrounded by a DZ. The comparison further illustrates that the phase time delay scheme is reliable regardless of the viscoelastic nature of the wave-induced deformation of the fracture in the presence of scattering and FPD effects.

The phase time delay method is important in the case study part, since the comparatively low amplitudes in the reference section in borehole SB1.1 rendered the transmission method impractical for this study. In general, the phase time delay method might be a more robust method for standard, production-type FWS data due to the repeatability of arrival times in consecutive logging runs and its independence of amplitudes, which are more prone to noise than the travel time characteristics. This may be particularly relevant when using this method for time lapse analysis of fracture compliance evolution or to assess the performance of hydraulic fracturing experiments. We note, however, that whenever the transmission method can be reliably applied, it can provide additional information about the energy dissipation prevailing at the fracture through the imaginary component of the fracture compliance. Another key message from this study is that, due to the presence of heterogeneity in the embedding host rock, one of the largest sources of uncertainty for the estimation of fracture compliance from FWS data is associated with the choice of a representative reference signal. To alleviate this problem, it is crucial

that a sufficient number of traces from the intact section of the formation is considered to obtain a representative reference signal.

Appendix A: Comparison of the Two Solutions of the Group Delay Method

The group delay method exhibits a non-monotonical relationship between the fracture-induced time delay and the fracture compliance, which leads to two possible solutions (Equation 6). Figure A1a shows the two compliance estimates for fractures with apertures of 1 and 5 mm embedded in a homogeneous background. For the 5 mm fracture, the two estimates are very similar, whereas they differ for the 1 mm case. For the latter, the solution with a negative sign in the square root of Equation 6 yields a compliance estimate (blue dot) that deviates considerably from the theoretical solution of the thin layer model (blue dashed horizontal line). To illustrate this ambiguity in the estimates, we compute the theoretical group time delays as a function of fracture compliance at 20 kHz using Equation 4. The results are shown in Figure A1b, where the blue and red asterisks correspond to the correct theoretical fracture compliance and group time delay for the fractures with apertures of 1 and 5 mm, respectively. The other possible solution of Equation 6 for the 1 mm fracture for the same group time delay produces a compliance estimate which is one order-of-magnitude larger. For the 5 mm fracture, the two possible solutions produce similar estimates, however, the estimated group time delays are larger than the theoretical maximum value (Figure A1b). This results in a negative term in the square root in Equation 6 and, consequently, leads to a complex-valued compliance estimate. In Figures 5 and A1, the real part of the compliances by group time delay method are shown, which still provide a good estimate for practical purposes. The underlying issue is that the phase difference for a 5 mm fracture is affected by scattering. By taking the derivative of the phase difference for the group time delay, the error is magnified and consequently leads to a breach of the theoretical limit. Nevertheless, for the phase and group time delay methods, the effect of scattering on the estimated compliance is negligible. In the absence of scattering effects, as for the 1 mm fracture case, the assumptions of the linear slip model are fulfilled, which results in both a better agreement with respect to the thin-layer model solution and a real-valued estimate of fracture compliance.
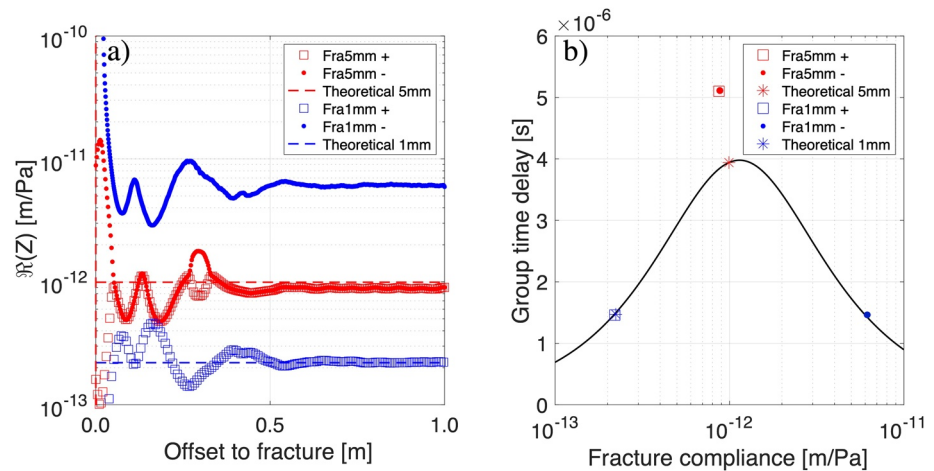
Figure A1. (a) Two solutions for the compliance estimate from the group time delay method for fractures with apertures of 1 mm (blue) and 5 mm (red). Square and dot symbols denote the solutions of Equation 6 with a positive and negative sign, respectively. The dashed horizontal lines denote the theoretical compliance of the thin layer model for two fractures. (b) Group time delay as a function of fracture compliance at a frequency of 20 kHz. The red and blue asterisks indicate the correct theoretical solution for the 5 and 1 mm cases, respectively. The dot and square correspond to the two possible solutions shown in the left Figure A1a.

Appendix B: Impact of Background Impedance on Fracture Compliance Estimation

For the stochastically heterogeneous background scenario in the numerical tests, we use the mean velocity and density to compute the background rock impedance required to estimate compliance (Equations 2, 6 and 7). To investigate the effect of the background rock impedance on the compliance estimation, we compute the

compliance of a 5 mm fracture in the homogeneous scenario for the maximum, minimum, and mean impedance values corresponding to the stochastically heterogeneous medium shown in Figure 2b. By doing so, the range of impedance values can be considered as an extreme scenario yet representative of the properties of the heterogeneous background model defining the magnitude of the observed time delays and amplitude decays. Figure B1 shows the compliance estimates with different impedances for all three methods, that is, the transmission, phase, and group time delay schemes. Table B1 illustrates the relative differences of compliance estimates with respect to the mean impedance case for receivers after the gray interference zone. Given the fracture compliance is an order-of-magnitude-type mechanical property, such small variations due to the rock impedance are negligible, which implies that the mean impedance values can be used to infer fracture compliance in heterogeneous environments.
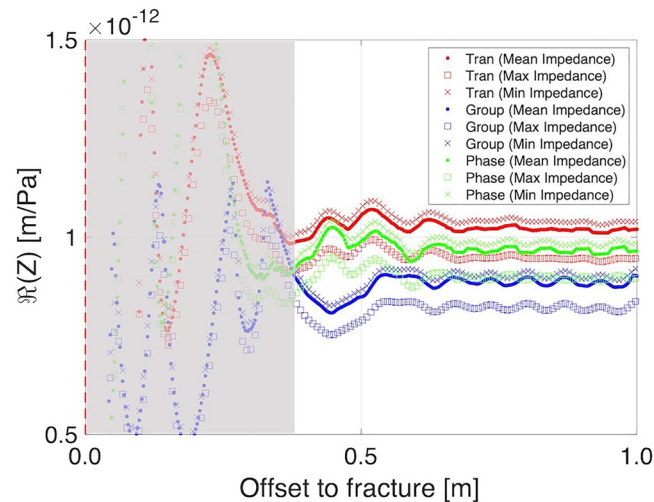
Figure B1. Comparison of compliance estimates for different background impedances for the fracture with an aperture of 5 mm. Red, blue, and green symbols denote fracture compliance estimates using the transmission, group, and phase time delay methods, respectively. Dot, square, and crossed symbols correspond to compliance estimates with the mean, maximum, and minimum impedances, respectively.

Table B1
Relative Differences of Compliance Estimates Computed From Maximum and Minimum Impedances With Regard to Those Obtained Using the Mean Impedance

	Transmission	Phase	Group
Max impedance (%)	7.4	6.3	8.0
Min impedance (%)	2.2	2.4	1.4

Data Availability Statement

The data for this study is available at https://doi.org/10.5281/zenodo.6245695.

References

Ahmadi, M., Taleghani, A. D., & Sayers, C. M. (2016). The effects of roughness and offset on fracture compliance ratio. *Geophysical Journal International*, *205*(1), 454–463. https://doi.org/10.1093/gji/ggw034

Aki, K., & Richards, P. G. (1980). *Quantitative seismology theory and methods*. W. H. Freeman and Company.

Bakku, S. K., Fehler, M., & Burns, D. (2013). Fracture compliance estimation using borehole tube waves. *Geophysics*, *78*(4), 249–260. https://doi.org/10.1190/geo2012-0521.1

Barbosa, N. D., Caspari, E., Rubino, J. G., Greenwood, A., Baron, L., & Holliger, K. (2019). Estimation of fracture compliance from attenuation and velocity analysis of full-waveform sonic log data. *Journal of Geophysical Research: Solid Earth*, *124*(3), 2738–2761. https://doi.org/10.1029/2018JB016507

Barbosa, N. D., Greenwood, A., Caspari, E., Dutler, N., & Holliger, K. (2021). Estimates of individual fracture compliances along boreholes from full-waveform sonic log data. *Journal of Geophysical Research: Solid Earth*, *126*(5), e2021JB022015. https://doi.org/10.1029/2021JB022015

Barbosa, N. D., Rubino, J. G., Caspari, E., Milani, M., & Holliger, K. (2016). Fluid pressure diffusion effects on the seismic reflectivity of a single fracture. *The Journal of the Acoustical Society of America*, *140*(4), 2554–2570. https://doi.org/10.1121/1.4964339

Barton, N. (2006). *Rock quality, seismic velocity, attenuation and anisotropy*. Taylor & Francis.

Biot, M. A. (1962). Mechanics of deformation and acoustic propagation in porous media. *Journal of Applied Physics*, *33*(4), 1482–1498. https://doi.org/10.1063/1.1728759

Bröker, K., & Ma, X. (2022). Estimating the least principal stress in a granitic rock mass: Systematic mini-frac tests and elaborated pressure transient analysis. *Rock Mechanics and Rock Engineering*, *55*(4), 1931–1954. https://doi.org/10.1007/s00603-021-02743-1

Caspari, E., Novikov, M., Lisitsa, V., Barbosa, N. D., Quintal, B., Rubino, J. G., & Holliger, K. (2019). Attenuation mechanisms in fractured fluid-saturated porous rocks: A numerical modelling study. *Geophysical Prospecting*, *67*(4), 935–955. https://doi.org/10.1111/1365-2478.12667

Clark, R. A., Benson, P. M., Carter, A. J., & Moreno, C. A. G. (2009). Anisotropic P-wave attenuation measured from a multi-azimuth surface seismic reflection survey. *Geophysical Prospecting*, *57*(5), 835–845. https://doi.org/10.1111/j.1365-2478.2008.00772.x

David, C., Nejati, M., & Geremia, D. (2020). *On petrophysical and geomechanical properties of Bedretto Granite*. ETH Zurich. https://doi.org/10.3929/ethz-b-000428267

Davies, R., Foulger, G., Bindley, A., & Styles, P. (2013). Induced seismicity and hydraulic fracturing for the recovery of hydrocarbons. *Marine and Petroleum Geology*, *45*, 171–185. https://doi.org/10.1016/j.marpetgeo.2013.03.016

Day-Lewis, F. D., Slater, L. D., Robinson, J., Johnson, C. D., Terry, N., & Werkema, D. (2017). An overview of geophysical technologies appropriate for characterization and monitoring at fractured-rock sites. *Journal of Environmental Management*, *204*, 709–720. https://doi.org/10.1016/j.jenvman.2017.04.033

Faulkner, D. R., Mitchell, T. M., Jensen, E., & Cembrano, J. (2011). Scaling of fault damage zones with displacement and the implications for fault growth processes. *Journal of Geophysical Research*, *116*(B5), B05403. https://doi.org/10.1029/2010JB007788

Foord, G., Verdon, J. P., & Kendall, J.-M. (2015). Seismic characterization of fracture compliance in the field using P- and S-wave sources. *Geophysical Journal International*, *203*(3), 1726–1737. https://doi.org/10.1093/gji/ggv395

Gassmann, F. (1951). Elastic waves through a packing of spheres. *Geophysics*, *16*(4), 673–685. https://doi.org/10.1190/1.1437718

Gischig, V. S., Giardini, D., Amann, F., Hertrich, M., Krietsch, H., Loew, S., et al. (2020). Hydraulic stimulation and fluid circulation experiments in underground laboratories: Stepping up the scale towards engineered geothermal systems. *Geomechanics for Energy and the Environment*, *24*, 100175. https://doi.org/10.1016/j.gete.2019.100175

Gutierrez, M., & Youn, D.-J. (2015). Effects of fracture distribution and length scale on the equivalent continuum elastic compliance of fractured rock masses. *Journal of Rock Mechanics and Geotechnical Engineering*, *7*(6), 626–637. https://doi.org/10.1016/j.jrmge.2015.07.006

Hertrich, M., Brixel, B., Broeker, K., Driesner, T., Gholizadeh, N., Giardini, D., et al. (2021). Characterization, hydraulic stimulation, and fluid circulation experiments in the Bedretto Underground Laboratory for Geosciences and Geoenergies. In *Paper presented at the 55th U.S. Rock Mechanics/Geomechanics Symposium, Virtual*.

Holliger, K. (1996). Upper-crustal seismic velocity heterogeneity as derived from a variety of *P*-wave sonic logs. *Geophysical Journal International*, *125*(3), 813–829. https://doi.org/10.1111/j.1365-246X.1996.tb06025.x

Holliger, K. (1997). Seismic scattering in the upper crystalline crust based on evidence from sonic logs. *Geophysical Journal International*, *128*(1), 65–72. https://doi.org/10.1111/j.1365-246X.1997.tb04071.x

Hunziker, J., Greenwood, A., Minato, S., Barbosa, N. D., Caspari, E., & Holliger, K. (2020). Bayesian full-waveform inversion of tube waves to estimate fracture aperture and compliance. *Solid Earth*, *11*(2), 657–668. https://doi.org/10.5194/se-11-657-2020

Li, Y. D., Rabbel, W., & Wang, R. (1994). Investigation of permeable fracture zones by tube-wave analysis. *Geophysical Journal International*, *116*(3), 739–753. https://doi.org/10.1111/j.1365-246x.1994.tb03294.x

Lissa, S., Barbosa, N. D., Rubino, J. G., & Quintal, B. (2019). Seismic attenuation and dispersion in poroelastic media with fractures of variable aperture distributions. *Solid Earth*, *10*(4), 1321–1336. https://doi.org/10.5194/se-10-1321-2019

Liu, E. (2005). Effects of fracture aperture and roughness on hydraulic and mechanical properties of rocks: Implication of seismic characterization of fractured reservoirs. *Journal of Geophysics and Engineering*, *2*(1), 38–47. https://doi.org/10.1088/1742-2132/2/1/006

Lubbe, R., Sothcott, J., Worthington, M. H., & McCann, C. (2008). Laboratory estimates of normal and shear fracture compliance. *Geophysical Prospecting*, *56*(2), 239–247. https://doi.org/10.1111/j.1365-2478.2007.00688.x

McClure, M. W., Jung, H., Cramer, D. D., & Sharma, M. M. (2016). The fracture-compliance method for picking closure pressure from diagnostic fracture-injection tests. *SPE Journal*, *21*(4), 1321–1339. https://doi.org/10.2118/179725-pa

Minato, S., & Ghose, R. (2016). AVO inversion for a non-welded interface: Estimating compliances of a fluid-filled fracture. *Geophysical Journal International*, *206*(1), 56–62. https://doi.org/10.1093/gji/ggw138

Möllhoff, M., & Bean, C. J. (2009). Validation of elastic wave measurements of rock fracture compliance using numerical discrete particle simulations. *Geophysical Prospecting*, *57*(5), 883–895. https://doi.org/10.1111/j.1365-2478.2008.00749.x

Möllhoff, M., Bean, C. J., & Meredith, P. G. (2010). Rock fracture compliance derived from time delays of elastic waves. *Geophysical Prospecting*, *58*(6), 1111–1122. https://doi.org/10.1111/j.1365-2478.2010.00887.x

Molyneux, J. B., & Schmitt, D. R. (2000). Compressional-wave velocities in attenuating media: A laboratory physical model study. *Geophysics*, *65*(4), 1162–1167. https://doi.org/10.1190/1.1444809

Müller, G., Roth, M., & Korn, M. (1992). Seismic-wave traveltimes in random media. *Geophysical Journal International*, *110*(1), 29–41. https://doi.org/10.1111/j.1365-246X.1992.tb00710.x

Nakagawa, S., & Schoenberg, M. A. (2007). Poroelastic modeling of seismic boundary conditions across a fracture. *The Journal of the Acoustical Society of America*, *122*(2), 831–847. https://doi.org/10.1121/1.2747206

National Research Council. (1996). *Rock fractures and fluid flow: Contemporary understanding and applications*. National Academic Press.

Ofterdinger, U., MacDonald, A. M., Comte, J.-C., & Young, M. E. (2019). Groundwater in fractured bedrock environments: Managing catchment and subsurface resources – An introduction. *Geological Society, London, Special Publications*, *479*(1), 1–9. https://doi.org/10.1144/SP479-2018-170

Pride, S. (2005). Relationships between seismic and hydrological properties. In *Hydrogeophysics* (pp. 253–290). Springer.

Prioul, R., & Jocker, J. (2009). Fracture characterization at multiple scales using borehole images, sonic logs, and walkaround vertical seismic profile. *AAPG Bulletin*, *93*(11), 1503–1516. https://doi.org/10.1306/08250909019

Pyrak-Nolte, L. J. (1996). The seismic response of fractures and the interrelations among fracture properties. *International Journal of Rock Mechanics and Mining Sciences & Geomechanics Abstracts*, *33*(8), 787–802. https://doi.org/10.1016/S0148-9062(96)00022-8

Pyrak-Nolte, L. J., & Morris, J. P. (2000). Single fractures under normal stress: The relation between fracture specific stiffness and fluid flow. *International Journal of Rock Mechanics and Mining Sciences*, *37*(1–2), 245–262. https://doi.org/10.1016/s1365-1609(99)00104-5

Pyrak-Nolte, L. J., Myer, L. R., & Cook, N. G. W. (1990). Transmission of seismic waves across single natural fractures. *Journal of Geophysical Research*, *95*(B6), 8617–8638. https://doi.org/10.1029/JB095iB06p08617

Pyrak-Nolte, L. J., & Nolte, D. D. (2016). Approaching a universal scaling relationship between fracture stiffness and fluid flow. *Nature Communications*, *7*(1), 10663. https://doi.org/10.1038/ncomms10663

Rubino, J. G., Castromán, G. A., Müller, T. M., Monachesi, L. B., Zyserman, F. I., & Holliger, K. (2015). Including poroelastic effects in the linear slip theory. *Geophysics*, *80*(2), 51–56. https://doi.org/10.1190/geo2014-0409.1

Rutqvist, J., & Stephansson, O. (2003). The role of hydromechanical coupling in fractured rock engineering. *Hydrogeology Journal*, *11*(1), 7–40. https://doi.org/10.1007/s10040-002-0241-5

Sayers, C. M. (2007). Introduction to this special section: Fractures. *The Leading Edge*, *26*(9), 1102–1105. https://doi.org/10.1190/1.2780777

Schmidt, P., Dutler, N., & Steeb, H. (2022). Importance of fracture deformation throughout hydraulic testing under *in situ* conditions. *Geophysical Journal International*, *228*(1), 493–509. https://doi.org/10.1093/gji/ggab354

Schoenberg, M. (1980). Elastic wave behavior across linear slip interfaces. *The Journal of the Acoustical Society of America*, *68*(5), 1516–1521. https://doi.org/10.1121/1.385077

Shapiro, S. A., & Dinske, C. (2009). Fluid-induced seismicity: Pressure diffusion and hydraulic fracturing. *Geophysical Prospecting*, *57*(2), 301–310. https://doi.org/10.1111/j.1365-2478.2008.00770.x

Sidler, R., Carcione, J. M., & Holliger, K. (2013). A pseudo-spectral method for the simulation of poro-elastic seismic wave propagation in 2D polar coordinates using domain decomposition. *Journal of Computational Physics*, *235*, 846–864. https://doi.org/10.1016/j.jcp.2012.09.044

Sidler, R., Carcione, J. M., & Holliger, K. (2014). A pseudospectral method for the simulation of 3-D ultrasonic and seismic waves in heterogeneous poroelastic borehole environments. *Geophysical Journal International*, *196*(2), 1134–1151. https://doi.org/10.1093/gji/ggt447

Sotelo, E., Rubino, J. G., Solazzi, S. G., Barbosa, N. D., & Holliger, K. (2021). Fractures in low-permeability rocks: Can poroelastic effects associated with damage zones enhance their seismic visibility? *Journal of Geophysical Research: Solid Earth*, *126*(5). https://doi.org/10.1029/2020JB021155

Tran, N. H., & Rahman, S. S. (2007). Development of hot dry rocks by hydraulic stimulation: Natural fracture network simulation. *Theoretical and Applied Fracture Mechanics*, *47*(1), 77–85. https://doi.org/10.1016/j.tafmec.2006.10.007

Tronicke, J., & Holliger, K. (2005). Quantitative integration of hydrogeophysical data: Conditional geostatistical simulation for characterizing heterogeneous alluvial aquifers. *Geophysics*, *70*(3), H1–H10. https://doi.org/10.1190/1.1925744

Vasconcelos, I., & Grechka, V. (2007). Seismic characterization of multiple fracture sets at Rulison Field, Colorado. *Geophysics*, *72*(2), 19–30. https://doi.org/10.1190/1.2436779

Vidal, J., & Genter, A. (2018). Overview of naturally permeable fractured reservoirs in the central and southern Upper Rhine Graben: Insights from geothermal wells. *Geothermics*, *74*, 57–73. https://doi.org/10.1016/j.geothermics.2018.02.003

Williams, J. H., & Johnson, C. D. (2004). Acoustic and optical borehole-wall imaging for fractured-rock aquifer studies. *Journal of Applied Geophysics*, *55*(1–2), 151–159. https://doi.org/10.1016/j.jappgeo.2003.06.009

Witherspoon, P. A., Wang, J. S. Y., Iwai, K., & Gale, J. E. (1980). Validity of Cubic Law for fluid flow in a deformable rock fracture. *Water Resources Research*, *16*(6), 1016–1024. https://doi.org/10.1029/WR016i006p01016

Worthington, M. H., & Lubbe, R. (2007). *Fractured reservoirs: The scaling of fracture compliance*. Geological Society. Special Publications.

Ye, Z., Janis, M., & Ghassemi, A. (2017). Laboratory investigation of permeability evolution in shear stimulation of granite fractures for EGS. In *Paper presented at the 41st GRC Annual Meeting, Salt Lake City, Utah*.